Proceedings of OMAE03
22ND International Conference on Offshore Mechanics and Arctic Engineering
June 8-13, 2003, Cancun, Mexico

OMAE2003-37340

FORCE-FEEDBACK CONTROL IN VIV EXPERIMENTS

Øyvind N. Smogeli
Dept. of Marine Technology
Norwegian University of Science and Technology
Otto Nielsens vei 10
N-7491 Trondheim, Norway
Email: smogeli@marin.ntnu.no

Franz S. Hover
Michael S. Triantafyllou
Dept. of Ocean Engineering
Massachusetts Institute of Technology
Cambridge, Massachusetts 02139
Email: [hover, mistetri]@mit.edu

ABSTRACT

A force-feedback control system for VIV experiments is designed and evaluated for the purpose of achieving high accuracy free vibration tests. Through an organized approach, this work details specific methods for minimizing the combined effect of mass and damping using control system fundamentals. The dynamics of the closed-loop system are analyzed, a numerical model constructed and a control scheme is chosen and implemented in real-time. The control system performance is evaluated by performing frequency response tests in air.

Free vibrations of a smooth aluminum cylinder are performed at Reynolds number 19000. Test series with damping ratios of one, two and five percent are performed, all with nondimensional mass four. A peak amplitude ratio of 1.15 is observed for the case of lowest damping. Forced vibration tests with the same setup are performed and compared to the free vibration results, giving consistent results.

Keywords: VIV, free vibrations, robotics.

INTRODUCTION

Flow around slender marine structures has been studied over several decades, and a multitude of experimental setups for VIV testing have been constructed, giving extensive knowledge on the details of vortex formations. Exhaustive information on this may be found in for example Sarpkaya [11], Bearman [2], Williamson and Roshko [14], Blevins [3], Gopalkrishnan [8], Brika and Laneville [4], Khalak and Williamson [10] and Govardhan and Williamson [9].

The main purpose of the present work was to develop a tool for performing VIV experiments at a high level of fidelity. The test apparatus is physically robust, and may be used in two ways: 1) For performing free vibration tests, where the cylinder is allowed to move freely in accordance with the fluid excitation forces. In this mode, the actual fluid forces on the cylinder are measured and used to drive a simulated second order system in real time, and the cylinder displaced according to the simulation. The focus of the current work is the control system designed for this purpose. 2) For forced vibration tests, where the cylinder is given a prescribed motion. The choice between free and forced vibration is made in software, and thus facilitates unique possibilities for comparison of free and forced vibration data on the exact same physical setup. Combining the real fluid forces with a simulated system gives large flexibility in the parameter space, as the damping ratio, natural frequency and mass ratio are chosen *in software only*, independent of the actual physical setup. It also facilitates realization of systems not achievable by a passive setup, and the ability to perform test series with variation in any parameter. By this work, the authors hope that the value of robotics in experimental hydrodynamics will earn increased recognition, as the applications in the intersection of classic hydrodynamics and robotics are challenging and in multitude. The hydrodynamic results presented here are only preliminary results with the newly developed control system. More exhaustive testing, encompassing a wider parameter space of for example varying mass ratios, varying Reynolds numbers and different VIV-suppressing methods may be performed

easily, due to the flexibility and robustness of the experimental setup.

In a more general setting, the ability to control the natural frequencies, mass and damping of a physical system means that the ratio of structural modes to the fluid modes, e.g. Karman vortex street formation or similar, can be controlled in real time. This has important applications in optimal thrust production with foils, galloping and energy extraction.

EXPERIMENTAL SETUP AND DATA PROCESSING

The present work was performed at the MIT Towing Tank with the "Virtual Cable Testing Apparatus", VCTA. The VCTA consists of a carriage running on steel rails at the length of the tank, a linear drive with a table moving in the vertical direction, a drive system and brushless motor connected to the linear drive and a computer with motor control and A/D boards. A rig consisting of a supporting beam, two struts with endplates and a test cylinder attached to the struts with load cells are mounted to the linear drive table. The tank dimensions are length 30 meter, width 2.5 meter and water depth 1.1 meter. The nominal vertical cylinder position is close to half the water depth.

Hover et al. [6] performed free vibrations of a cylinder at Reynolds number 3800, using a similar setup with force-feedback and a simulated system driving the cylinder in real time. A refit of the system, giving capabilities for testing at higher Reynolds numbers, has taken place since then. The current work is a thorough redesign of the control system, further exploring the capabilities of the VCTA.

Data postprocessing

The force coefficients are calculated in a postprocessing routine written in MatLab. The data acquisition was run at $400Hz$, and the postprocessing filter cutoff frequency was set to give amplitude distortions of less than 0.5 percent. The lift-force contains an inertial term due to the physical mass of the cylinder. This was corrected by twice differentiating the filtered position signal, multiplying with the cylinder mass and subtracting this from the measured force.

Motion and force are assumed to have a sinusoidal shape, with a phase lag of the force. The lift force is split in two: One term in phase with acceleration and one in phase with velocity:

$$y(t) = y_0 sin(\omega t) \tag{1}$$

$$F(t) = F_0 sin(\omega t + \phi) = F_a sin(\omega t) + F_v cos(\omega t) \tag{2}$$

Here, y_0 and F_0 are motion and force amplitudes respectively. To obtain the dimensionless force coefficients C_l, C_{lv} and C_{la}, the force amplitude can be divided by the dynamic pressure $p_d = 0.5\rho LDU_0^2$, with ρ the density of water, L and D the cylinder length and diameter, and U_0 the towing velocity. The time dependent force $C_f(t)$ can then be written dimensionless as:

$$C_f(t) = \frac{F(t)}{p_d} = C_l sin(\omega t + \phi) = -C_{la} sin(\omega t) + C_{lv} cos(\omega t) \tag{3}$$

The two coefficients C_{lv} and C_{la} are computed from the force time series using inner products:

$$C_{lv} = \sqrt{\frac{2}{T}} \frac{< C_f(t), \dot{y}(t) >}{\sqrt{< \dot{y}(t), \dot{y}(t) >}} \tag{4}$$

$$C_{la} = \sqrt{\frac{2}{T}} \frac{< C_f(t), \ddot{y}(t) >}{\sqrt{< \ddot{y}(t), \ddot{y}(t) >}} \tag{5}$$

T represents the window length for the inner product. The window length is set equal to one oscillation period, and coefficients calculated for each period in the test run. The final coefficient values are are then given by mean and standard deviation of these.

The added mass coefficient C_m and the damping ratio ζ may be deduced from the coefficients defined above. C_m can be calculated from C_{la}, ω, y_0 and U_0. The damping ratio ζ is directly related to the lift force in phase with velocity C_{lv}, and may also be deduced from the force amplitude F_0 and phase ϕ:

$$C_m = \frac{-C_{la} \frac{1}{2} \rho LDU_0^2}{\omega^2 y_0 \rho \frac{\pi}{4} D^2 L} = \frac{-2C_{la}U_0^2}{\pi D \omega^2 y_0} \tag{6}$$

$$\zeta = \frac{LDU_0^2 C_{lv}}{4\omega y_0 \omega_n \nabla m^*} = \frac{F_0 sin(\phi)}{2y_0 \omega \omega_n \rho \nabla m^*} \tag{7}$$

SYSTEM IDENTIFICATION AND MODELLING

Controller and drive system

The computer running the real-time simulation is mounted on the VCTA carriage. It is equipped with an A/D board and a motor control board (later referenced as the MEI). The motor is controlled by giving velocity commands, which are calculated from the simulated dynamics. The command velocity is integrated by the board controller, and the axis output voltage V_c is calculated from a PD servo control algorithm with parameters K_p and $K_d \delta t$ operating on the position error $e = y_d - y$. The servo loop on the MEI board runs at a much higher frequency than the control loop, and is in the analysis viewed as continuous. The commanded torque is given by $Q_c = k_v V_c$ with k_v the gain. The

drive system has a time constant T_m, and is modelled as a first order system. The linear drive has a gear ratio k_m. The backlash in the linear drive was found to be approximately 1.0mm, but analysis of the results indicated that the backlash did not have a significant effect on the dynamics. This may be due to the high damping in the slide. The encoder count from the motor is used as position feedback, with a gain k_{enc}. The transfer function from position error to motor force F_m can then be written:

$$\frac{F_m}{e} = \frac{k_v k_{enc}(K_p + K_d \delta t s)}{k_m(1 + T_m s)} \tag{8}$$

The math and input/output operations in the control code give rise to a computational delay between reading of the feedback force and the velocity command. The computational delay τ is modelled together with the drive system time lag by a 2nd order Padé-approximation after the controller output $\hat{y}_d$, giving the actual desired position y_d.

$$\frac{y_d}{\hat{y}_d} = \frac{s^2 + \frac{6}{\tau}s + \frac{12}{\tau^2}}{s^2 + \frac{6}{\tau}s - \frac{12}{\tau^2}} \tag{9}$$

The rig

The rig is mounted to the linear slide, and consists of a bracket holding a supporting beam, two struts with mounting pins and the test cylinder. The rig is supported by a spring, so that the sum force of gravity G and spring F_s can be written as $F_s + G = K_0 y$, with K_0 the spring constant and y the position.
A model of the rig, capturing the flexure in the supporting beam and test cylinder, was established by using conventional beam theory. The test cylinder is modelled as a simply supported beam with mass M_{c1}, stiffness K_{c1} and damping B_{c1}, and a uniform load from inertial effects due to accelerations of the beam endpoints. The supporting beam is modelled as a cantilever beam with a point mass on the end with mass M_{b1}, stiffness K_{b1} and damping B_{b1}. Combining the above models into a complete rig model was done by defining an equivalent mechanical system. The equivalent system consists of three masses connected by springs and dampers. The system has three degrees of freedom, one for each mass displacement: y,y_c and y_b. Figure 1 shows a schematic of the rig and the equivalent system.

Omitting the argument s, the resulting transfer functions from motor force to the positions are:

$$\frac{y}{F_m} = \frac{a_2 a_3 - b_2^2}{a_1 a_2 a_3 - a_1 b_2^2 - a_3 b_1^2} \tag{10}$$

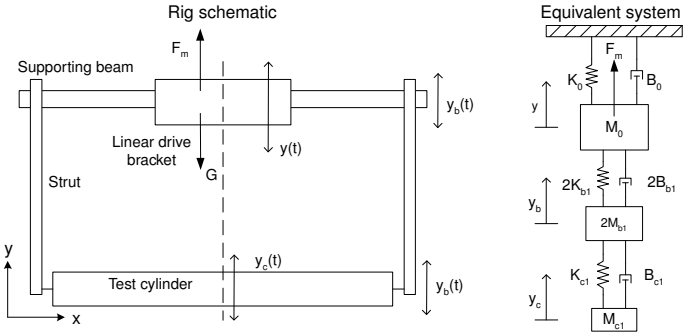

Figure 1. Rig schematic and equivalent mechanical system

$$\frac{y_b}{F_m} = \frac{y}{F_m}\frac{b_1 a_3}{a_2 a_3 - b_2^2} = \frac{b_1 a_3}{a_1 a_2 a_3 - a_1 b_2^2 - a_3 b_1^2} \tag{11}$$

$$\frac{y_c}{F_m} = \frac{y_b}{F_m}\frac{b_2}{a_3} = \frac{b_1 b_2}{a_1 a_2 a_3 - a_1 b_2^2 - a_3 b_1^2} \tag{12}$$

$$a_1 = M_0 s^2 + (B_0 + 2B_{b1})s + (K_0 + 2K_{b1}) \tag{13}$$

$$a_2 = 2M_{b1}s^2 + (2B_{b1} + B_{c1})s + (2K_{b1} + K_{c1}) \tag{14}$$

$$a_3 = M_{c1}s^2 + B_{c1}s + K_{c1} \tag{15}$$

$$b_1 = 2K_{b1} + 2B_{b1}s \tag{16}$$

$$b_2 = K_{c1} + B_{c1}s \tag{17}$$

The structural model predicts natural modes at 4, 158, 226 and 333 rad/s. The modes at 4 and 333rad/s are well damped, and not possible to recognize in the dynamic response. The most important natural modes were found at ~ 140 and $\sim 240 rad/s$. The model agrees fairly well, although the two modes at 158 and 226rad/s are closer together than the observed modes.

Force feedback

The force on the test cylinder is measured by two Kistler piezo-electric quartz load cells. The dynamics of the force sensors are neglected in the model, but in modelling the system, the introduction of structural inertia in the measurements must be accounted for. As the system is oscillating, the force sensors will pick up a force component due to accelerations of the cylinder structural mass. This comes in addition to the fluid forces. The inertial component F_i and transfer function from cylinder position to F_i is written as:

$$F_i(t) = -[M'_{c1}(\ddot{y}_c - \ddot{y}_b) + M_c \ddot{y}_b] \tag{18}$$

$$\frac{F_i}{y} = \frac{-s^2[(M_c - M'_{c1})b_1 a_3 + M'_{c1} b_1 b_2]}{a_2 a_3 - b_2^2} \tag{19}$$

M_c is the rigid-body cylinder mass and M'_{c1} is a vibrational mass of the same kind as M_{c1}. If the vibrational modes are neglected

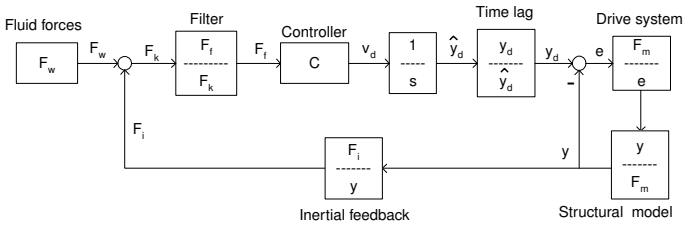

Figure 2. VCTA block diagram

by setting $y_c = y_b = y$, the remaining term corresponds to the inertial term generated by the rigid-body cylinder due to the cylinder motion y. The Kistler amplifiers of type 5010B convert the sensor signal from charge to an analog voltage, and filter the forces at $33Hz$. The frequency response of the amplifiers was found to match that of a 3rd order Butterworth filter. The normalized transfer function for the Butterworth filter, from measured force at the Kistlers, F_k, to the feedback force F_f, is given as:

$$\frac{F_f(s)}{F_k(s)} = \frac{1}{f_0 s^3 + f_1 s^2 + f_2 s + f_3} \tag{20}$$

Combined dynamics

Using the controller C and the transfer functions F_f/F_k, $y_d/\hat{y}_d$, F_m/e, y/F_m and F_i/y defined in equations 20, 9, 8, 10 and 19, the dynamics can be expressed in a simple block diagram. This can be found in Fig. 2.

A further simplification, which removes the MEI feedback loop, can be made by establishing a transfer function including the whole drive system, $y/y_d(s)$:

$$\frac{y}{y_d} = \frac{\frac{F_m}{e}\frac{y}{F_m}}{1 + \frac{F_m}{e}\frac{y}{F_m}} \tag{21}$$

The complete dynamics expressed in one transfer function from the water forcing F_w to bracket position y is written as:

$$\frac{y}{F_w} = \frac{\frac{F_f}{F_k}\frac{F_m}{e}\frac{y}{F_m}\frac{y_d}{\hat{y}_d}\frac{1}{s}C}{1 + \frac{F_m}{e}\frac{y}{F_m} - \frac{F_f}{F_k}\frac{F_m}{e}\frac{y}{F_m}\frac{F_i}{y}\frac{y_d}{\hat{y}_d}\frac{1}{s}C} = \frac{\frac{F_f}{F_k}\frac{y}{y_d}\frac{y_d}{\hat{y}_d}\frac{1}{s}C}{1 - \frac{F_f}{F_k}\frac{y}{y_d}\frac{F_i}{y}\frac{y_d}{\hat{y}_d}\frac{1}{s}C} \tag{22}$$

This transfer function is of order 15.

The simulated system

For the current work, the desired system to be simulated is chosen as a 2nd order mass-damper-spring system written in terms of the mass ratio m^*, commanded damping ratio ζ_c, natural frequency ω_n and displaced water volume ∇, here given as a transfer function from fluid forcing F_w to cylinder position y :

$$\frac{y}{F_w}(s) = \frac{\frac{1}{\rho\nabla m^*}}{s^2 + 2\zeta_c\omega_n s + \omega_n^2} \tag{23}$$

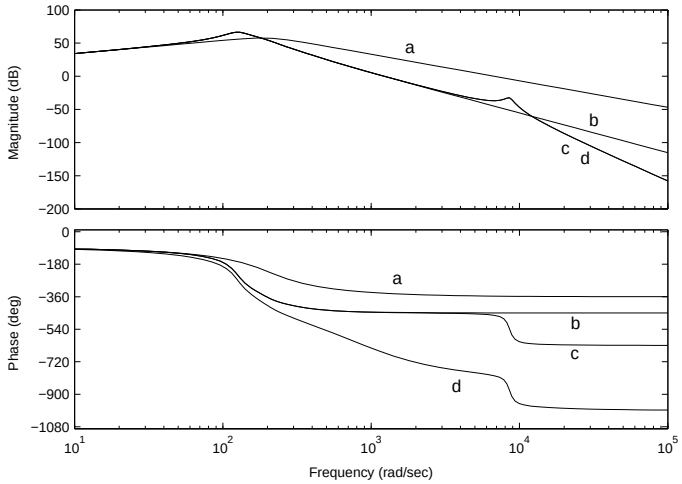

Figure 3. Frequency response of the VCTA plant model. a: Only the filter model, b: Filter and structural model, c: Filter, structural and drive system model, d: Full model.

Model verification and results

Figure 3 shows a Bode diagram of the plant model. The complete plant transfer function is from commanded velocity v_c to filtered inertial feedback force F_{fi}:

$$\frac{F_{fi}}{v_c} = \frac{1}{s}\frac{y_d}{\hat{y}_d}\frac{y}{y_d}\frac{F_i}{y}\frac{F_f}{F_k} \tag{24}$$

This excludes the effect of fluid forcing F_w, which is viewed as an external perturbation of the system. The Bode diagram contains five different systems marked “a” to “d”. “a” is the force filter model alone, i.e. $y/\hat{y} = 1, y/y_d = 1$ and $F_i/y = -M_c s^2$. “b” is the force filter and structural model, i.e. $y/\hat{y} = 1$ and $y/y_d = 1$. “c” is the force filter, structural and drive system model, i.e. $y/\hat{y} = 1$. “d” is the full plant model.

For evaluation of the closed-loop transfer function (CLTF) model given by Eq. 22, a control algorithm must be included. The control algorithm used models the dynamics given in Eq. 23 and accounts for the inertial term in the feedback force. By using an exact inertia correction, the discrepancy between the closed-loop model and the desired dynamics will be given solely by the

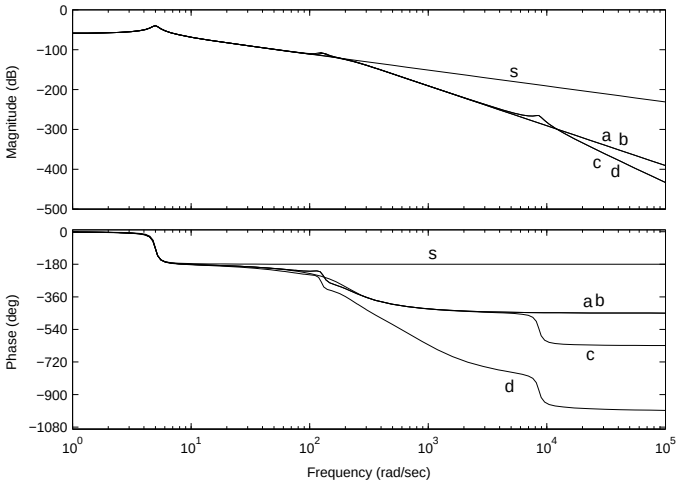

Figure 4. Frequency response of the CLTF

modelled system dynamics. The dynamics presented here is for $m^* = 4$, $\omega_n = 5 rad/s$ and $\zeta = 0.05$. Figure 4 shows a Bode diagram with with five different systems marked "a" to "d" and "s". "s" is the desired dynamics, and "a" to "d" are the closed-loop transfer functions when accounting for different elements of the dynamics, as used in the plant description in Fig. 3.

Since the force filter is included in all the models, the cutoff frequency of at $33Hz = 207 rad/s$ is clearly seen in all the magnitude plots, and also as the midpoint of a 270 degree phase loss for the "a" model in the phase plot. The addition of the structural modes is seen as a small change in amplitude and phase over a limited area from approximately 50 to 300 rad/s. The magnitude of the contribution is dependent on the structural mode damping ratio, which is a uncertainty in the model. The inclusion of the drive system model does not give any significant contribution to the dynamics below 4000 rad/s. This addition is seen as the "c" model branching off from "a" and "b" in both magnitude and phase. The addition of the time delay in drive and computation, seen in line "d", gives a clear contribution to the phase for all frequencies, but is not seen in the magnitude plot. Figure 5 shows a detail of the experimental area, and reveals that only the filter model and the time delay are contributing to any significant change in phase.

CONTROLLER DESIGN AND TESTING

The purpose of the control design process was to create a controller that would give the closed-loop system the properties of a second-order mass-spring-damper system. Loopshaping was chosen as control design approach. This method is described in Åström and Wittenmark [1] and Doyle et al. [5], and was used also by Hover and Triantafyllou [7]. The general idea of loopshaping can be illustrated as follows: Given a closed-loop system transfer function $L(s)$ and a desired dynamic response $S(s)$,

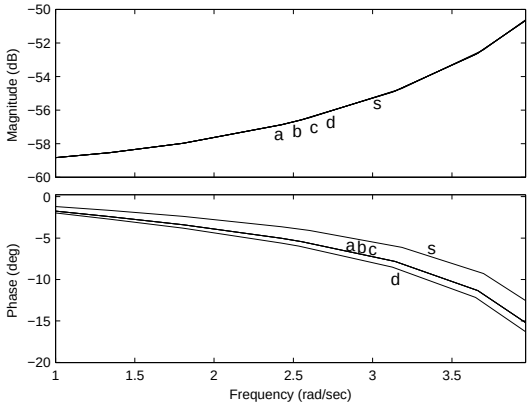

Figure 5. Detail of CLTF below the natural frequency

design the controller $C(s)$ so that $L(s) \simeq S(s)$ in the interesting interval of s.

For the system in question, $L(s)$ is the closed-loop transfer function from fluid forcing $F_w(s)$ to the cylinder position $y(s)$, and $S(s)$ can for the time being be defined as a second-order mass-spring-damper system. Setting $\frac{y}{F_w} = S$ and solving Eq. 22 for C gives:

$$C = \frac{S}{\frac{F_f}{F_k}\frac{y}{y_d}\frac{1}{s}[1 + S\frac{F_i}{y}]} \tag{25}$$

The order of the controller will be the sum of the orders of the dynamic model and the desired dynamics. The by far most significant dynamic component for low frequencies is the force filter, so a compensation for this is a natural part of the controller. The structural mode model has contributions located around 100 rad/s. The structural modes introduce no significant phase at low frequencies, so in the light of the desired controller properties, they need not be included in the controller as long as they no not interfere with the system stability. The motor and board model give no significant contributions to the dynamics below 4000 rad/s, and are naturally left out of the controller. The computational delay is also neglected, since the phase introduced by this is small compared to the filter phase. In a future refinement, it is desired to include also this phase lag in the controller. The controller transfer function then becomes:

$$\begin{aligned} \frac{y}{y_d} &= 1 \\ \frac{F_f}{F_k} &= \frac{1}{f_0 s^3 + f_1 s^2 + f_2 s + f_3} \\ \frac{F_i}{y} &= -\hat{M}_c s^2 \end{aligned}$$

$$C(s) = \frac{f_0 s^4 + f_1 s^3 + f_2 s^2 + f_3 s}{\frac{1}{S(s)} - \hat{M}_c s^2} \tag{26}$$

If $S(s)$ is specified as a second order mass-spring-damper system with parameters M, B and K, the controller becomes:

$$C(s) = \frac{f_0 s^4 + f_1 s^3 + f_2 s^2 + f_3 s}{(M - \hat{M}_c)s^2 + Bs + K} \tag{27}$$

This controller polynomial has the expected form, consisting of a second order system with reduced simulated mass due to the inertial compensation, and force filter inversion. Since the numerator is of higher order than the denominator, this transfer function is not proper, and hence not suitable as a controller. To make the transfer function proper, extra rolloff at high frequencies was added. This also aids in noise attenuation. To increase flexibility and tuning options, two second order systems with independent natural frequencies and damping ratios were added to the desired dynamics, giving an additional fourth order rolloff. To avoid the rolloff affecting the dynamics significantly, the natural frequencies should be as high as possible and the damping ratios low. The rolloff polynomials $r_i(s)$ ($i = \{1,2\}$) and the new controller polynomial was specified as :

$$r_i(s) = \frac{s^2}{\omega_{ri}^2} + 2\zeta_{ri}\frac{s}{\omega_{ri}} + 1 \tag{28}$$

$$C(s) = \frac{f_0 s^4 + f_1 s^3 + f_2 s^2 + f_3 s}{(Ms^2 + Bs + K)r_1(s)r_2(s) - \hat{M}_c s^2} \tag{29}$$

This controller was chosen for implementation and testing. The rolloff natural frequencies ω_{ri} were chosen as 100 and $120Hz$, and the damping ratios ζ_{ri} chosen as 0.5 and 0.3.

The continuous time controller transfer function was discretized by Tustin's approximation and implemented in polynomial form. Care was taken to assure correct timing of the control loop, as to not corrupt the performance of the control system. Error-checking throughout the control code was included, so that desired real-time performance could be validated for each run.

Phase lag and damping

A phase lag in the system will effectively be seen as damping. The phase ϕ between force and position of a general second-order system can be written as:

$$\phi = tan^{-1}\left(\frac{-2\zeta\frac{\omega}{\omega_n}}{1 - \frac{\omega^2}{\omega_n^2}}\right) \tag{30}$$

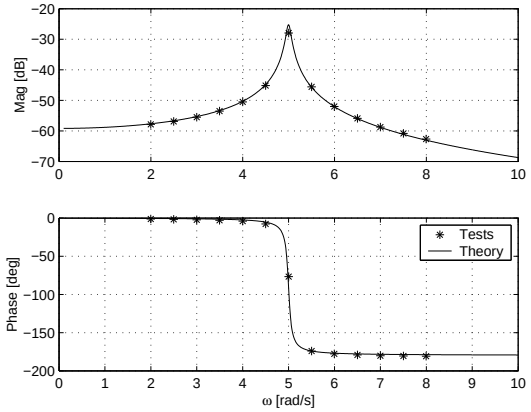

Figure 6. Bode diagram for $\omega_n = 5 rad/s$, $\zeta_c = 0.01$

For frequencies below the natural frequency of the system, the phase lag is small and approximately linear in the forcing frequency. If this phase is added to another system, it may be viewed as a phase lag $\delta\phi$ due to a pure time delay τ, giving rise to the added damping ratio $\delta\zeta$. Combined with the small angle identity for the tangent function this gives:

$$\delta\zeta \approx \frac{\delta\phi(\frac{\omega^2}{\omega_n^2} - 1)}{2\frac{\omega}{\omega_n}} = \frac{\tau}{2}\omega_n(\frac{\omega^2}{\omega_n^2} - 1) = \frac{\tau}{2}\omega_{mod} \tag{31}$$

This expression shows that the introduced damping ratio is linear in the modified frequency ω_{mod}, given a linear phase.

Frequency response

Extensive tests were performed to determine the frequency response characteristics of the system. To remove the effect of fluid forces, the tank was drained for water. With the cylinder in air, the only term in the force feedback loop was the cylinder inertial force. An external force was generated in software and filtered to get the same phase lag as the actual force, and added to the feedback force from the force sensors. This total force then drove the system as in normal free vibrations.

Frequency response tests were performed for 5 different simulated systems: $\omega_n = 5$ with ζ_c=0.05, 0.01 and 0.00 and ζ_c=0.01 with $\omega_n = 3$ and 7. For each system, forcing frequencies from 2 to 8 rad/s were tested and at least 50 steady-state oscillations included in the postprocessing. Figure 6 shows test results for a simulated system with $\zeta_c = 0.01$ and $\omega_n = 5$ as stars, with the desired second-order system drawn as a continuous line.

The controller worked properly for varying damping and natural frequency, and gave consistent results for very low commanded damping. However, the desired system dynamics are

not exactly met. The desired natural frequency and motion magnitude are achieved with high precision, but the phase deviates a little from that of the desired system. From the model results presented above, this was to be expected, since the controller does not account for the phase from the time lag. According to the discussion on phase and damping, the phase discrepancy gives rise to a varying damping ratio. To investigate this, the system damping ratio ζ_s was calculated from the lift force coefficient in phase with velocity, C_{lv}. Figure 7 shows the variation of ζ_s and the damping ratio discrepancy $\delta\zeta = \zeta_s - \zeta_c$ versus the modified frequency ω_{mod} for the same tests.

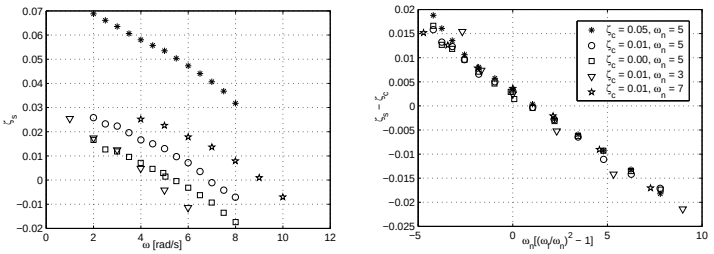

Figure 7. System damping ratio $\zeta_s$versus forcing frequency (left) and damping ratio discrepancy $\zeta_s - \zeta_c$versus ω_{mod}(right) for all frequency response runs

It is clear that ζ_s varies with up to 2 percent for a given ζ_c in the given frequency interval, and that $\delta\zeta$ line up nicely to a straight line in ω_{mod}. As shown previously, *this corresponds to a time delay in the system*. By including all the dynamics in the system model, and using the controller defined in this chapter, the model may be used to predict the controller performance. Figure 8 shows a detail of experimental results with $\zeta_c = 0.01$ compared to the model prediction and the desired system.

The model predicts the actual phase lag seen in the experiments to a high degree. Using the model to predict the introduced damping, the resulting correction line is almost perfectly linear and agrees well with the experimental results.

Damping ratio correction

An attempt was made to correct the commanded damping ratio ζ_c in order to achieve a desired system damping ratio ζ_s. For a specific run, this involved assuming the forcing frequency to be known, finding the damping ratio correction $\delta\zeta$ from a curve fit to the results in figure 7 and then subtracting $\delta\zeta$ from ζ_s to find ζ_c. To test the effect of making such a correction, runs with a desired ζ_s of 0.0018 were performed. The measured damping ratios were found to be within the interval 0.018 ± 0.003, which is a large improvement over the constant ζ_c runs.

The tradeoff in using the damping ratio correction is a small

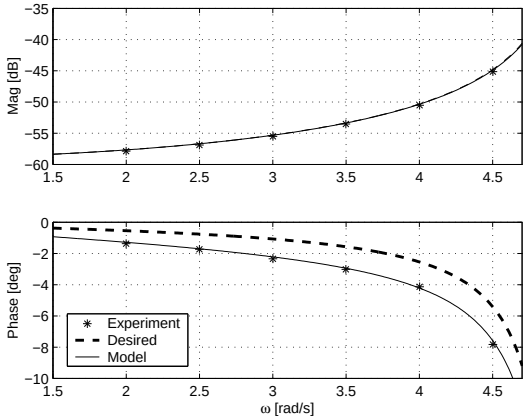

Figure 8. Experiments compared to model and desired system for $\zeta_c = 0.01$ below ω_n

magnitude distortion. In changing the commanded damping ratio, the phase is changed to yield the desired system damping, but in the same process the magnitude of the frequency response is changed.

For the frequency response tests, ω_{mod} could easily be calculated, since both ω_n and ω_f are known. For free vibrations, this is not so, and an alternative method had to be formulated. The chosen approach is to perform initial tests with constant ζ_c, and find the relation of ω_n to ω_f for the range of reduced velocities to be tested with constant ζ_s. This can be done because the natural frequency changes very little with the change in damping in question here. Having established an experimental curve of the relationship between ω_n and ω_f, ω_{mod} may be calculated for any V_{rn} covered by the span in ω_n. The damping ratio correction $\delta\zeta$ is then used to find ζ_c from ζ_s. This approach assumes that the fluid forcing is mainly sinusoidal, and of consistent frequency between runs. In reality the forcing is broadband, so it is only at the main frequency the damping ratio will be exactly correct. The variation is however small, as shown in the frequency response tests earlier.

Pluck tests

Pluck tests in air were performed to further validate the system performance. The system was run in free vibration mode, and perturbed by displacing the cylinder. The decay of the cylinder was logged and analyzed. For zero commanded damping, the actual damping ratio calculated from the logarithmic decay was found to be approximately 0.002, which in this case is also equal to $\delta\zeta$. This result agrees fairly well with the expected damping ratio from the frequency response tests, which was approximately 0.003. Pluck tests with other commanded damping ratios gave the same damping ratio discrepancy as the zero case.

Suggestion for an improved controller

The performance of the controller used in this work is good, but further improvements may be possible. The discrepancy from the desired performance has been shown to be due to a time lag in the system, of which the controller is not compensating for. If the controller could compensate for this time lag, the system phase would be exactly that of the desired system, and no additional damping ratio would be introduced. Two possible ways of achieving this are presented here.

Additional lead compensation may be added to the controller in form of a first-order system. The controller transfer function would then have the following form:

$$C(s) = \frac{(f_0 s^4 + f_1 s^3 + f_2 s^2 + f_3 s)}{(Ms^2 + Bs + K) r_1(s) r_2(s) - \hat{M}_c s^2} \frac{s+W}{W} \qquad (32)$$

Where W is the tuning parameter for the lead compensation. It was found that $W = 180 rad/s$ would cancel out the phase from the time lag for low frequencies. The magnitude is unaffected. This controller has the same order numerator and denominator.

Another way of modifying the controller is to change the butterworth filter model. If the cutoff frequency in the filter compensation is decreased from $33Hz$, more phase will be taken out at low frequencies. Setting cutoff at $23.5Hz$ will cancel out the phase from the time lag for low frequencies. This approach gives no change to the controller transfer function, but will affect phase and magnitude of the closed loop around the cutoff frequency. This may lead to problems, since the affected frequency is close to the natural modes of the structure.

Even with the phase from the time lag being compensated for, some phase is still introduced in the controller due to the added rolloff-terms. Since the rolloff was chosen as high as possible without giving problems with stability, it is doubtful that more phase may be compensated for without affecting the stability. If any of the above modifications were to be tried out, careful tuning of the system would be necessary. Using the current control system design (i.e. loopshaping), we believe that the system is being pushed close to the limit of its capabilities.

RESULTS

The towing speed for the tests was chosen as $0.25 m/s$, which with a cylinder diameter of $0.0762m$ gives $Re \approx 19000$. The kinematic viscosity ν has been estimated to $1E-6 m^2/s$. Tests were run for system natural frequencies from 2 to 8 rad/s, which corresponds to nominal reduced velocities V_{rn} from 2.6 to 10.3

49 test runs were performed with ζ_c of 5 and 2 percent for the whole range of natural frequencies. From these results, a test matrix for constant ζ_s of 5, 2 and 1 percent was established, and tests were again run for V_{rn} from 2.6 to 10.3. In total, 75 new runs were done.

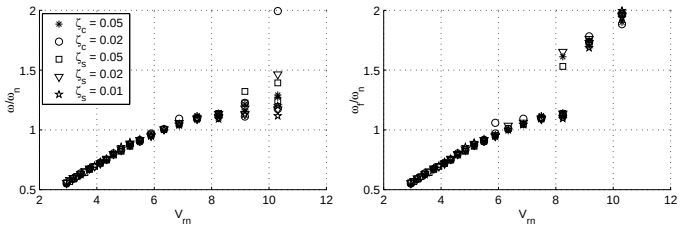

Figure 9. Forcing and motion frequency ratio to commanded natural frequency

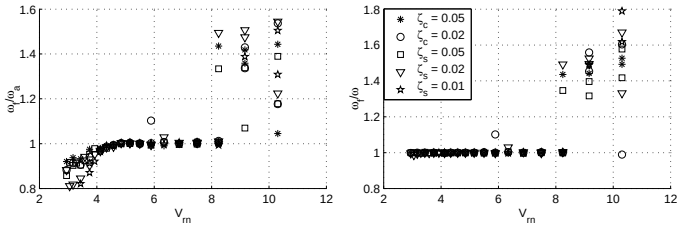

Figure 10. Forcing versus actual natural frequency and motion frequency

Processing of the free vibration data showed the largest amplitudes for V_r from 5.50 to 6.25. 10 forced vibration runs each at V_r 5.50, 5.75, 6.00 and 6.25 were done for comparison with the free vibrations.

Lock-in and oscillation frequencies

Figures 9 and 10 shows the relationships between main forcing frequency ω_f, motion frequency ω, system natural frequency ω_n and actual natural frequency included added mass ω_a.

ω_a can be found from ω_n by using the experimentally determined added mass coefficient:

$$\omega_a = \omega_n \sqrt{\frac{m^*}{m^* + C_m}} \qquad (33)$$

Lock-in is shown as a horizontal line of $\omega_a/\omega_f = 1$. For lower frequencies (high V_{rn}), the calculations are more uncertain, and the data points are scattered.

Standard deviations for $\zeta_s = 0.01$

The test series with constant system damping ratio of 1 percent has been used as an indication of the standard deviation for the rest of the results, with plus/minus one standard deviation plotted as vertical lines for all data points.

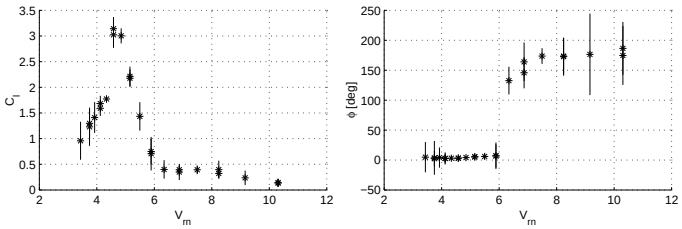

Figure 11. C_l and ϕ with standard deviation for ζ_s = 0.01

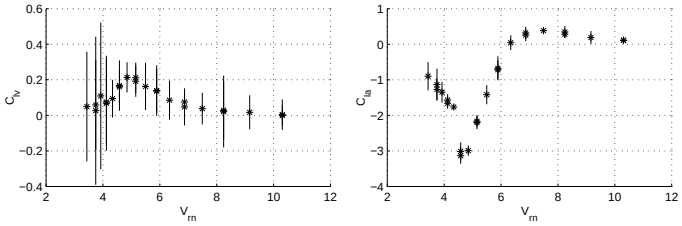

Figure 12. C_{lv} and C_{la} with standard deviation for ζ_s = 0.01

Figure 11 shows the total lift coefficient C_l and phase ϕ. The standard deviation of the phase for low frequencies is large. This is because the time series for these runs were irregular, and no proper steady-state sinusoidal oscillation was reached, giving uncertain coefficient calculations. This can also be seen by the repeated tests, which turn out somewhat dissimilar for high V_{rn}. For the rest of the V_{rn} span, the standard deviations are reasonable, and the repeated tests show good repeatability. In the lock-in region the standard deviations are small, and repeated tests almost identical.

Figure 12 shows lift coefficients in phase with velocity and acceleration: C_{lv} and C_{la}. The standard deviation of C_{lv} is large, but the repeated tests show good agreement. Standard deviations of C_{la} are of the same magnitude.

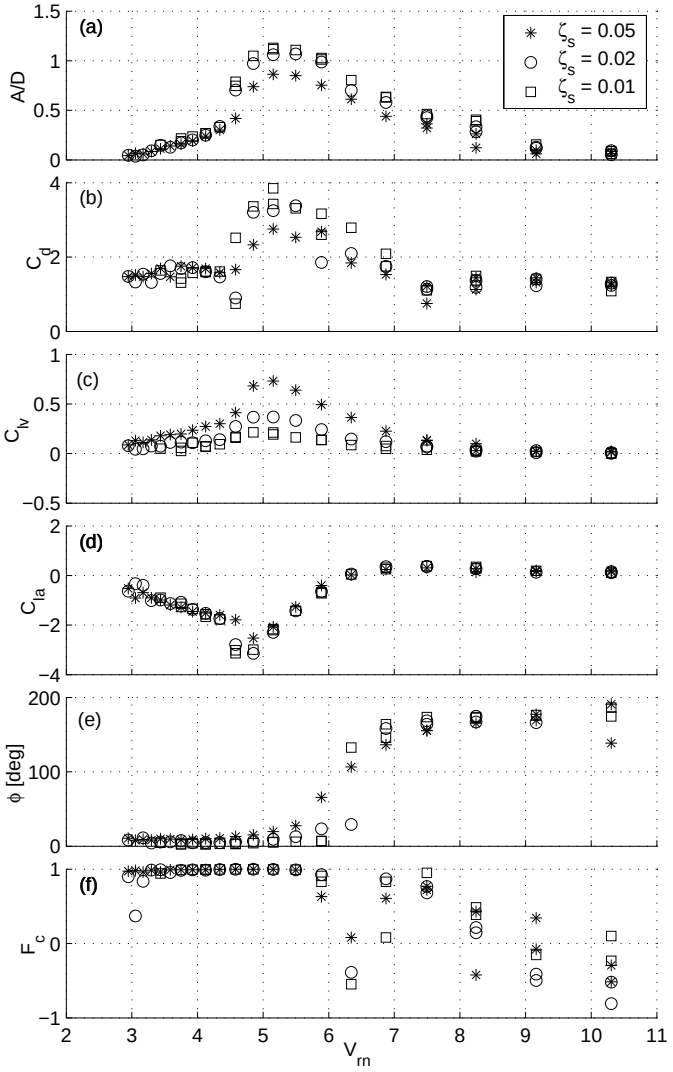

Figure 13. Free vibration results versus V_{rn} for ζ_s = 0.01, 0.02 and 0.05

The cases ζ_s = 0.01, 0.02 and 0.05

Figure 13 shows amplitude ratio A/D (a), drag coefficient C_d (b), lift in phase with velocity C_{lv} (c), lift in phase with acceleration C_{la} (d), phase angle ϕ (e) and force correlation coefficient F_c (f) versus V_{rn} for ζ_s = 0.01, 0.02 and 0.05. A few wild points for ϕ at high V_{rn} have been removed from the plot. Figure 14 shows the same results plotted versus V_r.

The phase exhibits the expected behavior, with a shift at at approximately $V_{rn} \approx 6$. This corresponds to a natural frequency of 3.4 rad/s. C_{la} lies approximately on the same curve for all damping ratios, reaching a minimum of -3 for V_{rn} just below 5. The plot of C_{lv} shows large differences between the damping ratios. The shapes of the curves are approximately the same, reaching maximum at $V_{rn} \approx 5$. The peaks seems to be shifted a little up in V_{rn} with increasing damping ratio. The peak values for damping ratios 0.05, 0.02 and 0.01 are respectively 0.75, 0.38 and 0.21. The C_d plot is more irregular than the other plots, but shows the same general shape as the lift force plots. The maximum drag occurs at V_{rn} = 5 for all damping ratios. The amplitude ratio reaches maximum a little above V_{rn} = 5. The maximum values for ζ_s = 0.05, 0.02 and 0.01 are 0.85, 1.1 and 1.15. F_c is exactly 1 for V_{rn} from 3.7 to 5.5. Between 5.5 and 6.5, the correlation drops suddenly, but increases again for V_{rn} up to 8. Here it drops off again, showing no clear pattern for any of the damping ratios. Viewed together with the standard deviation, which was discussed in the previous section, this is consistent with results from Hover et al. [6].

The results from the test series with constant ζ_s were compared to the results from the corresponding ζ_c series. The differences between the runs are small, but some observations may be made. The values of C_{lv} for the lower range of V_{rn} are larger

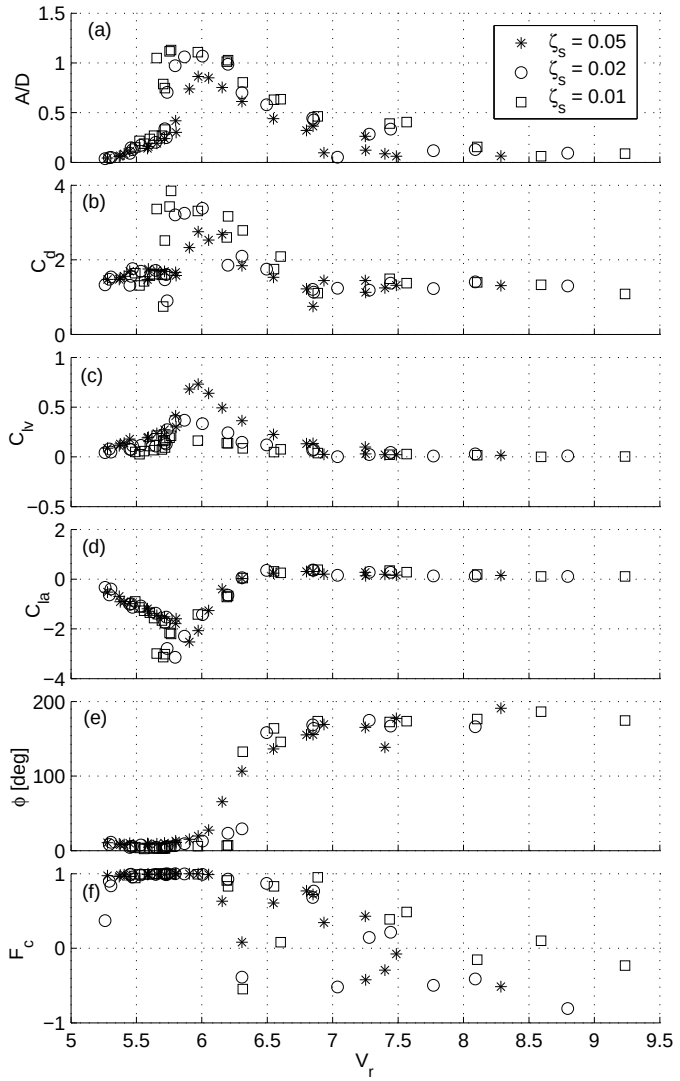

Figure 14. Free vibration results versus V_r for ζ_s = 0.01, 0.02 and 0.05

for the constant ζ_c runs. This is consistent with the actual system damping ratio being higher than desired. The peak amplitudes are slightly larger for the constant ζ_s runs. This consistent with the amplitude distortion introduced by modifying the commanded damping ratio.

Forced vibration results

The peak oscillation amplitudes in free vibrations occur for reduced velocities V_r between 5.75 and 6. To test the free vibration results, a set of forced vibration tests were run for $V_r = 5.5$, 5.75, 6.0 and 6.25 with varying amplitude. Figure 15 shows C_{lv} versus A/D for all values of V_r. It it interesting to notice that the curves for V_r 5.75 and 6.00 cross zero for A/D 1.1 - 1.15. The zero-crossing of C_{lv} marks the point at which the fluid neither gives or takes energy from the system; for positive values it absorbs energy from the system (thus damping it), whereas for negative values it helps excite the system. This point should then correspond to the point of maximum amplitude in free vibrations, which is exactly what is seen here. This is a convenient confirmation of the free vibration results, and also shows that forced vibrations is a good model for predicting free vibrations. The picture is not so clear for the V_r cases of 5.5 and 6.25. The first of these lines predict no motion above $A/D = 0.1$, but in free vibration approximately 0.2 is found. The second line predicts a maximum A/D of 0.9, whereas the free vibrations gave 1.0. There are clearly some uncertainties in the experiments, but in total the forced vibration results agree fairly well with the free vibrations. A further comparison between forced and free vibration results was made by extracting values of C_{lv} and A/D for constant V_r of 5.75, 6.00 and 6.25. The three damping ratios thus yielded three points for each value of V_r. These points are plotted with C_{lv} from the forced vibrations in Fig. 15. The points for V_r = 6 shows excellent agreement, whereas the points for V_r = 5.75 and 6.25 are less accurate, though still in reasonable agreement.

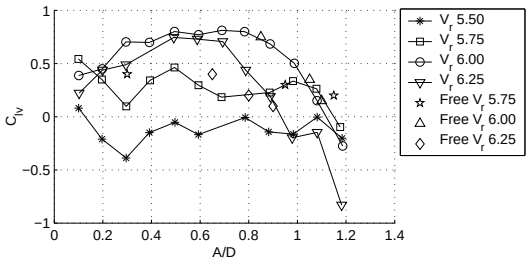

Figure 15. Comparison of C_{lv} vs. A/D for forced and free vibration results

COMPARISON WITH PREVIOUS RESULTS

Previous free vibration results with a similar test setup were performed by Hover et al. [6]. An interesting discrepancy from the current data can be found for V_r from 6 to 8. In the data from Hover et al., there is here clearly an area of almost constant amplitude, or "knee", which is not seen in the present data. Similar differences between apparently similar experimental setups have been noticed before, and are discussed in Khalak and Williamson [10].

Khalak and Williamson [10] and Govardhan and Williamson [9] have performed extensive tests using a cantilever cylinder in a flow channel. Their results indicate two types of response, depending on the magnitude of the combined mass-damping parameter ($m^*\zeta$). For high ($m^*\zeta$), two amplitude branches are distinguished, separated by a discontinuous mode transition, while low ($m^*\zeta$) gives an additional branch and two mode transitions.

The results presented here do not show any clear response branches or discontinuous mode transitions. This also applies

to the results by Hover et al. [6]. A passive setup described in Vikestad [13] and Skaugset and Larsen [12] produces results similar to the ones described here. Vikestad used a light cylinder, with mass ratio 1.66 and damping ratio approximately 0.8, got maximum amplitude ratios of approximately 1.15 for V_{rn} 6 and observed a slight "knee" in the response, although much smaller than the one observed by Hover et al. Skaugset and Larsen had a mass ratio of 2.96 and damping ratio 1.9 percent. They got slightly smaller amplitudes and a did not see the "knee". Their results agree well with the ones presented here for the whole range of reduced velocities. The reason for these discrepancies between experimental setups is unclear, and should be subject to further investigation.

CONCLUSIONS

An essential conclusion of this work is the usefulness of applied robotics in fluid mechanics. It has been shown that a force-feedback control system using a robust mechanical setup can achieve remarkably low levels of mass-damping, comparable to the lowest achieved by any passive system presented in literature. Compared to a passive system, the complexity increases due to the force-feedback loop and control system. The most important gain is however the flexibility in changing the system parameters at will, and that the verification of the system performance may be done in general terms, covering a wide parameter space. The ability of changing the system natural frequency also enables free vibration tests over a range of reduced velocities at constant Reynolds number, as the flow velocity is kept constant between runs.

The focus of the present work has been on design and evaluation of the feedback control system, and the free vibration tests were only extensive enough to give preliminary conclusions. The results show that further testing with the system should be carried out, covering a wider parameter space and investigating the Reynolds-number dependability of the results. This might also shed some light on the different responses experienced with different experimental setups.

REFERENCES

[1] Åström, K.J. and Wittenmark, B., 1997, "Computer-controlled systems", Prentice-Hall Inc., New Jersey, 3rd ed.

[2] Bearman, P.W., 1984, "Vortex shedding from oscillating bluff bodies", Annual review of Fluid Mechanics, **16**, pp. 195-222.

[3] Blevins, R.D., 1990, "Flow-induced vibration", Krieger Publishing Company, Florida, 2nd ed.

[4] Brika, D. and Laneville, A., 1993, "Vortex-induced vibrations of a long flexible circular cylinder", J. Fluid Mech., **250**, pp. 481-508.

[5] Doyle, J.C. et.al, 1992, "Feedback control theory", Macmillan Publishing Company, New York.

[6] Hover, F.S. et.al, 1998, "Forces on oscillating uniform and tapered cylinders in crossflow", J. Fluid Mech., **363**, pp. 97-114.

[7] Hover, F.S. and Triantafyllou, M.S., 2000, "Combined simulation with real-time force feedback: A new tool for experimental fluid mechanics", in System theory: Modeling, analysis and control(Ed. Djaferis, T.E. and Schick, I.C.), Kluwer Academic Publishers, Boston.

[8] Gopalkrishnan, R., 1993, "Vortex-induced forces on oscillating bluff cylinders", PhD Thesis, Massachusetts Institute of Technology/Woods Hole Oceanographic Institute Joint Program in Oceanographic Engineering.

[9] Govardhan, R. and Williamson, C.H.K, 2000, "Modes of vortex formation and frequency response of a freely vibrating cylinder", J. Fluid Mech., **420**, pp. 85-130.

[10] Khalak, A. and Williamson, C.H.K., 1996, "Dynamics of a hydroelastic cylinder with very low mass and damping", J. Fluid Mech., **10**, pp. 455-472.

[11] Sarpkaya, T. ,1979, "Vortex-induced oscillations", J. Applied Mech., **46**, pp. 241-258.

[12] Skaugset, K. B. and Larsen, C. M., 2002, "Suppression of vortex induced vibrations of circular cylinders using radial water jets", Proceedings of OMAE2002, Oslo, Norway, OMAE2002-28095.

[13] Vikestad, K., 1998, "Multi-frequency response of a cylinder subjected to vortex shedding and support motions", Dr.ing. thesis, Department of Marine Structures, NTNU, Trondheim.

[14] Williamson, C.H.K. and Roshko, A., 1988, "Vortex formation in the wake of an oscillating cylinder", J. Fluid Struct., **2**, pp. 355-381.